Available online at www.sciencedirect.com
ScienceDirect
Journal of Catalysis 250 (2007) 85–93
JOURNAL OF CATALYSIS
www.elsevier.com/locate/jcat

Promotion of the long-term stability of reforming Ni catalysts by surface alloying

Eranda Nikolla, Johannes Schwank, Suljo Linic *

Department of Chemical Engineering, 2300 Hayward Street, University of Michigan, Ann Arbor, MI 48109, USA

Received 29 January 2007; revised 12 April 2007; accepted 21 April 2007

Available online 2 July 2007

Abstract

Carbon-induced catalyst deactivation is one of the main problems associated with the electrocatalytic and catalytic reforming of hydrocarbons over supported Ni catalysts. We have used DFT calculations to study various aspects of carbon chemistry on Ni surfaces. We demonstrate that the carbon tolerance of Ni can be improved by synthesizing Ni-containing surface alloys that, compared to monometallic Ni, preferentially oxidize C atoms rather than form C–C bonds and have a lower thermodynamic driving force, associated with the nucleation of carbon atoms on low-coordinated Ni sites. Using the molecular insights obtained in the DFT calculations, we have identified Sn/Ni surface alloy as a potential carbon-tolerant reforming catalyst. The predictions of the DFT calculations were supported by our reactor and catalyst characterization studies, which showed that Sn/Ni is much more resistant to carbon poisoning than monometallic Ni in the steam reforming of methane, propane, and isooctane at moderate steam-to-carbon ratios.

Keywords: Hydrocarbon reforming; SOFC; Carbon poisoning; Ni alloys; DFT; Sn/Ni; Rational catalyst design

1. Introduction

Steam reforming (rxn1) is an endothermic catalytic process involving the conversion of hydrocarbons and water into hydrogen and oxidized carbon. The reaction is usually accompanied by a slightly exothermic water-gas shift process (rxn2),

$$C_nH_m + nH_2O \rightarrow nCO + (n + m/2)H_2 \text{ (rxn1)},$$

$$CO + H_2O \rightarrow CO_2 + H_2 \text{ (rxn2)}.$$

Besides being a crucial process for the catalytic hydrogen production, steam reforming is also important in direct electrochemical hydrocarbon reforming over solid oxide fuel cells (SOFCs) [1,2]. SOFCs are devices that generate electricity by electrochemically oxidizing various fuels, such as hydrogen, CO, and hydrocarbons. One of the main issues associated with the electrocatalytic and catalytic reforming of hydrocarbons is that commonly used catalysts, such as Ni supported on oxides, deactivate due to the formation of carbon deposits [3–6]. The carbon-induced catalyst deactivation can be suppressed by increasing the feed steam concentration [3]. High steam concentration is not desirable, because additional heat is required to heat and vaporize water. This approach is also not optimal for SOFCs, because higher inlet steam concentration results in lower energy density [7]. The need for the steam introduction also requires additional system components, complicating fuel cell system integration.

Several attempts have been made to identify carbon-tolerant steam-reforming catalysts [5,6,8–11]. For example, it has been suggested that Ru and Rh do not facilitate the formation of carbon deposits due to poor carbon solubility in these metals [12,13]. However, Ru and Rh are prohibitively expensive. It has also been shown that small amounts of sulfur can suppress carbon poisoning by blocking carbon nucleation sites [14,15]. Similarly, quantum chemical density functional theory (DFT) calculations have predicted that Au/Ni surface alloys should exhibit better carbon tolerance than monometallic Ni [16,17]. These predications have been verified experimentally [6,16,17]. In addition, it has also been shown that Cu supported on ceria is a stable electrooxidation catalyst for the internal reforming of hydrocarbons [18–20]. These materials operate at lower tem-

* Corresponding author. Fax: +1 734 764 7453.
E-mail address: linic@umich.edu (S. Linic).

0021-9517/$ – see front matter
doi:10.1016/j.jcat.2007.04.020

peratures compared to the Ni-based electrocatalysts due to the inferior thermal stability of Cu, thermal incompatibility of ceria and YSZ, and poor thermal stability of ceria [21–24].

In this contribution, we have utilized DFT calculations to study the factors that govern the stability of Ni-based reforming catalysts. We demonstrate that monometallic Ni deactivates due to the high rates of C–C bond formation and the high thermodynamic driving force associated with the nucleation and growth of extended carbon structures. DFT calculations also show that Sn/Ni surface alloys, with small amount of Sn alloyed into the Ni surface layers, should be more carbon-tolerant than monometallic Ni. Furthermore, our DFT calculations illustrate that in the limit of low Sn concentrations, the formation energy of the Sn/Ni surface alloy is lower than the formation energies associated with the bulk mixing of Sn and Ni and the separate Sn and Ni phases. The predictions of the DFT calculations are supported by reactor tests performed under the conditions corresponding to the internal on-cell reforming over SOFC anodes. We have also performed various catalyst characterization studies, including scanning electron microscopy (SEM), transmission electron microscopy (TEM), scanning transmission electron microscopy (STEM), energy-dispersive X-ray spectroscopy (EDS), X-ray diffraction (XRD), and X-ray photoelectron spectroscopy (XPS).

2. Methods

2.1. Density functional theory

The Dacapo pseudopotentials plane wave code (http://www.camp.dtu.dk) was used for all calculations. Our approach was to find a set of parameters that ensured the relative convergence, that is, the convergence of the respective energies of various structures. With this set of parameters, we have been able to reproduce various properties, such as carbon atom adsorption energies, oxygen adsorption energies, graphene sheet adsorption energy on Ni(111), and an activation barrier for the attachment of a C atom to the graphene sheet over Ni(111) reported previously by others [14,25,26]. For the Ni(111) model system, we use 3×3 supercells with 4-layer slabs and 18 special Chadi–Cohen k-points. The calculations for the (211) termination surfaces were performed using 1×3 supercells with 9-layer slabs and $3 \times 3 \times 1$ Monkhorst–Pack k-points. Six layers of vacuum separated the slabs, and a dipole-correction scheme was used to electrostatically decouple the slabs. The GGA-PW91 functional was employed for self-consistent spin-polarized electronic structure calculations. Vanderbilt pseudopotentials were used to describe core electrons. The density of valence electrons was determined self-consistently by iterative diagonalization of Kohn–Sham Hamiltonian using Pulay mixing of densities. The plane wave basis set used to describe the one-electron states was cut off at 350 eV. An electronic temperature (k_bT) of 0.1 was used during calculations, with the final results extrapolated to 0 K. In the geometry optimization calculations on the (111) surface termination, the two top substrate layers and adsorbates were allowed to fully relax. On the (211) termination, the three top substrate layers were alloyed to relax in the x (normal to the direction if the step-edge) and z directions. The forces were minimized to 0.05 eV/A.

The first-order transition states for one-atom diffusion on a surface were identified by probing the high-symmetry sites between reactant and product states. The diffusing atom was fixed in the x–y plane on these sites and was allowed to relax in the z direction. Energies were calculated for all high-symmetry sites (hollow, bridge, and on-top), and the potential energy surfaces were constructed. The identity of the first-order transition states was validated by making sure that the forces acting on the system vanish at the transition state and that the force on the diffusing atom changes sign as it moves through the transition state from the reactant to the product state. The transition states were further validated by slightly changing the geometry of the transition state along the reaction coordinate toward the product or reactant geometry and allowing the system to fully relax into the respective product and reactant states [27]. This procedure established that the transition state energies are maximum along the reaction coordinate and minimum with respect to other degrees of freedom [28–30]. The forces in these calculations were minimized to 0.05 eV/A. Transition states for the C–O and C–C bond formation were identified using the climbing nudged elastic band method [31–33].

2.2. Catalyst synthesis

Yttria-stabilized zirconia (8 mol%) was prepared via a coprecipitation method [34]. A mixture of yttrium nitrate [$Y(NO_3)_3{\cdot}6H_2O$] and zirconyl chloride ($ZrOCl_2{\cdot}2H_2O$) in deionized water was precipitated using a solution of ammonium hydroxide. After filtration and drying overnight, the precipitate was calcined at 1073 K for 2 h. The Ni supported on YSZ catalyst was synthesized by ball milling a mixture of NiO (Alfa Aesar) and 8 mol% YSZ in methanol for 24 h. Once dried, the powder was pressed into 13-mm-diameter pellets at 5000 psi. The pellets were then heated to 1673 K at a rate of 2 K/min and sintered for 4 h. The catalyst was reduced at 1173 K for 5 h using 30% H_2/N_2 to insure full reducibility of the pellets.

Sn was introduced to the sintered pellets via the incipient wetness technique using $SnCl_2{\cdot}4H_2O$ to obtain the desired Sn loading. The pellets were dried overnight at 473 K and then reduced under 400 sccm stream of 30% H_2/N_2 for 5 h at 1173 K.

2.3. BET surface area measurements

Single-point BET analysis was used to measure the surface area of the YSZ support via N_2 adsorption. The surface areas of the Ni/YSZ and Sn/Ni/YSZ catalysts were measured using N_2 physisorption at 77 K and H_2 chemisorption at 373 K. The physisorption and chemisorption experiments were conducted using Quantachrome's ChemBet 3000 equipped with thermal conductivity detectors (TCDs). The catalyst was first reduced under 30% H_2/N_2 at 1173 K for 5 h. After the reduction treatment, the sample was cooled under pure N_2 to 373 K, and the H_2 chemisorption studies were conducted at this temperature. These experiments yielded almost identical surface areas for

the Ni/YSZ and Sn/Ni/YSZ alloy catalysts for identical metal loadings.

2.4. Temperature-programmed reduction

The TPR experiments were conducted with the ChemBet (3000). Approximately 0.1 g of a catalyst (Ni/YSZ, Sn/Ni/YSZ, or unsupported Sn) was loaded in a U-tube reactor. The temperature was ramped at 10 K/min from 298 to 1173 K under 30% H_2/N_2. The TCD signal was detected via the Quantachrome data acquisition system.

2.5. X-ray diffraction

The XRD measurements were conducted with a Cu$K\alpha$ source using a Philips XRG5000 3-kW X-ray generator with crystal alignment stage and a Rigaku thin film camera. The spectrum was analyzed using Jade v.7 software.

2.6. X-ray photoelectron spectroscopy

The XPS experiments were conducted using a Kratos Axis Ultra XPS with a 150-W Al (Mono) X-ray gun. This instrument was operated ex situ under a pressure of 5×10^{-9} Torr. Fresh and used samples were pressed on an indium foil and left under vacuum overnight. The runs were conducted using pass energies of 40 and 20 eV. The charge neutralizer was used to prevent sample charging. The instrument was calibrated with respect to Au $4f_{7/2}$ at 84 eV.

2.7. Scanning transmission electron microscopy, transmission electron microscopy, and energy-dispersive X-ray spectroscopy

A Joel 2010F electron microscope was used for the STEM, TEM, and EDS studies. The instrument was operated at 200 kV under a pressure of 1.5×10^{-7} Torr. The instrument is equipped with a zirconated tungsten (100) thermal field emission tip filament. The EDS measurements were performed with the Ametec EDAX system, integrated in the microscope, in spot and scanning modes. To obtain a reasonable current, the lens was set for a probe size of 0.5 nm. The elemental scanning images were obtained using 512×512 pixels in a frame at a dwell time of 200 ms. To minimize the effect of specimen drift, a drift correction mode was used during the elemental mapping. For each sample, several particles from several different areas were analyzed.

2.8. Reactor studies

The reactor experiments were conducted isothermally at 1073 K in a packed-bed reactor setup. The setup includes a set of mass flow controllers, a pair of thermocouples (inside and outside the reactor), and peristaltic pumps for liquid delivery. Approximately 0.8 g of catalyst (active material plus support in both powder and pellet form) and a total inlet gas flow rate of 1400 sccm were used. Gas feeds were delivered with mass flow controllers, and liquid fuels and water were supplied via peristaltic pumps. The reactor effluent was analyzed using a Varian gas chromatograph (Varian CP 3800) equipped with a TCD.

3. DFT studies

The elementary-step mechanism of hydrocarbon steam reforming on Ni has been studied by many investigators [3,26,35]. It is generally accepted that a hydrocarbon decomposes over Ni, forming carbon and hydrogen adsorbates [14,35,36]. Carbon is removed from the catalyst surface in oxidation reactions forming CO and CO_2. Oxidizing agents (O and OH) are formed on Ni in the process of steam activation. In addition to reacting to form CO and CO_2, the C atoms and fragments also react with each other, forming extended carbon networks, such as graphene sheets or nanotubes, which deactivate the catalyst. This is illustrated in Fig. 1a, where it is shown that a catalytic particle of Ni is completely covered by carbon deposits after steam reforming of propane at the steam-to-carbon ratio of 1.5. The proposed mechanism is further supported by Fig. 1b, which shows the DFT-calculated reaction energies for various elementary steps involved in methane steam reforming on Ni(111). Similar results were obtained by others [14,35]. The DFT calculations in Fig. 1b show that there are two thermodynamically stable states for C atoms: (i) CO, which is formed in the process of the C atoms oxidation and, (ii) extended car-

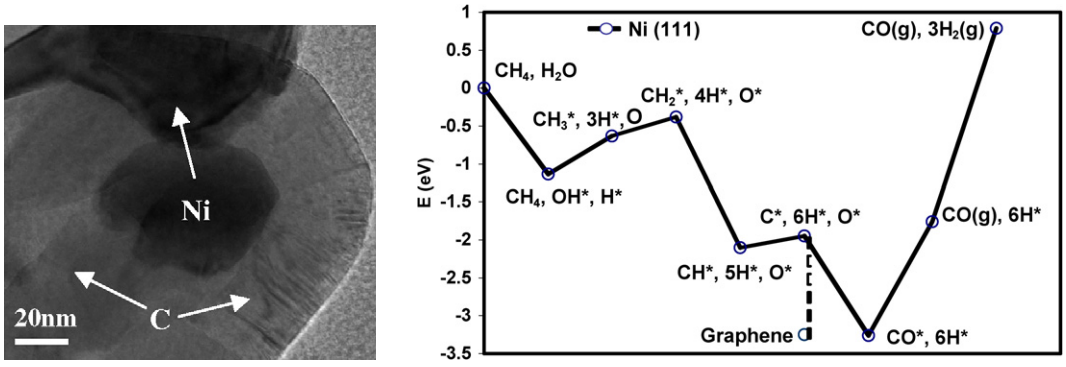

(a) (b)

Fig. 1. (a) Transmission electron micrograph of a Ni particle covered by carbon. The carbon deposits are formed in the process of propane steam reforming at 1073 K and at a steam-to-carbon ratio of 1.5. (b) DFT-calculated reaction energies for various elementary steps in steam reforming of methane on Ni(111).

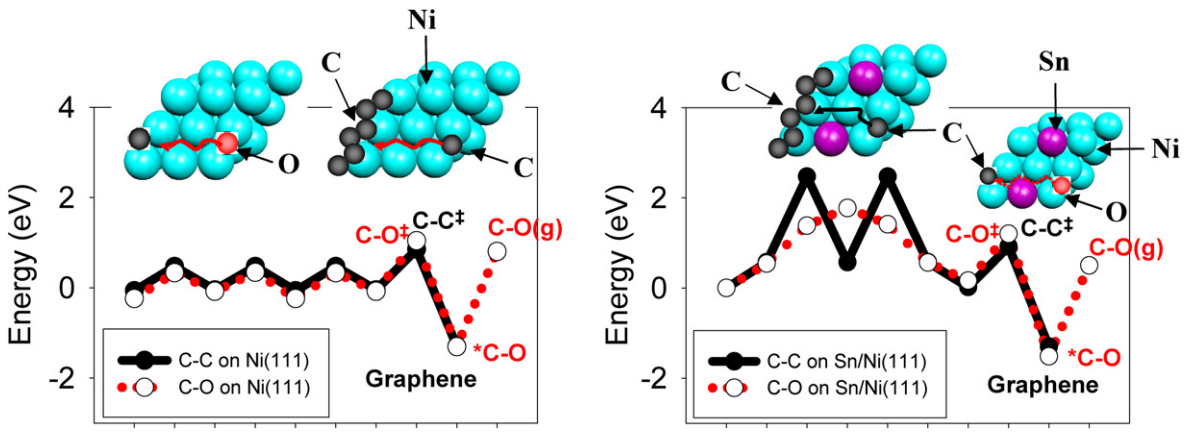

Fig. 2. DFT-calculated reaction energies for C–C and C–O bond formation on (a) Ni (111) and (b) Sn/Ni (111) surface alloy. The C–C bond formation is modeled as a C atom diffusing on the surface, approaching, and reacting with a carbon nucleation center. The nucleation center is modeled as a chain of carbon atoms adsorbed in the most stable structure (as calculated with DFT) on the (111) surfaces. The C–O bond formation is modeled as an O atom diffusing on the surface, approaching, and reacting with the C atom adsorbed in a three-fold hollow site. Inserts show the lowest energy reaction pathways. The energies for the C and O atom diffusion at the sites that are removed from the carbon nucleation center and an adsorbed C atom respectively were computed in a (3×3) unit cell with single C or O atom in the unit cell. The energies for the elementary C–C and C–O bond formation reactions on Ni and Sn/Ni were computed in the (3×3) unit cell with C and O atoms (in the reactant state) positioned at the 3-fold hollow site which is closest to the carbon nucleation center and to the C atom respectively. Ni is depicted as large blue (light) atom, Sn is large magenta, C is small black (dark), and O is small red (light). Red lines and letters correspond to O diffusion and the C–O bond formation, while black lines and letters correspond to C diffusion and the C–C bond formation.

bon network (graphene) formed in the process of the C–C bonds formation. The formation of extended carbon structures on Ni has received significant attention [6,25,37]. For example, recent in situ TEM studies have demonstrated that theese carbon structures are formed in the process of C atoms diffusion over the surface of Ni particles and subsequent attachment to a carbon nucleation center [37]. It has been shown that carbon nucleates on the undercoordinated sites of Ni [37]. The analysis of Fig. 1 suggests that any carbon-tolerant catalyst should be able to efficiently oxidize C atoms while preventing the formation of C–C bonds; that is, the oxidation of C atoms is a prerequisite for their removal from the surface via either CO desorption or the water-gas shift reaction to form CO_2(g) [34].

It has been shown previously that the formation of carbon deposits can be suppressed by modifying the Ni catalyst surface (surface alloying), so that the rate of the C–C bond formation is adversely affected. These molecular insights have led to the identification of Au/Ni surface alloy, which exhibited improved carbon tolerance in the steam reforming of various hydrocarbons [16,34].

The problem of carbon poisoning can also be formulated in terms of the selectivity associated with the formation of C–C versus C–O bonds. In a previous contribution, we have used this rationalization to identify Sn/Ni surface alloys as possible carbon-tolerant alternative to monometallic Ni [34]. These findings are presented in Fig. 2, which shows the DFT-calculated potential energy surface associated with the oxidation of a C atom and the potential energy surface for the attachment of a C atom to a carbon nucleation center. The nucleation center was modeled as a chain of carbon atoms adsorbed in the equilibrium configuration, on the (111) surface of pure Ni and the Sn/Ni surface alloy. The Sn/Ni surface alloy is characterized by the Sn atoms displacing the Ni atoms from the top Ni(111) layer. Fig. 2 suggests that whereas on Ni(111) the potential energy surfaces associated with the C–C and C–O bond formation are very similar to each other, on the Sn/Ni surface alloy the overall activation barrier for the C atom oxidation is much lower (by ∼1 eV for the given model system) than the overall activation barrier associated with the C–C bond formation. The change in the overall activation barrier is a consequence of the increased barriers for the C atom diffusion. The hindered C diffusion leads to the lower rates of the C–C bond formation. On the other hand, the O atom diffusion is hindered to a lesser degree, and the rates of C–O bond formation are affected less. These studies indicate that the Sn/Ni surface alloy should, compared to Ni, preferentially oxidize C atoms rather than form C–C bonds and thus should have a higher resistance toward the formation of extended sp2 carbon networks [34].

We note that Sn/Ni catalysts have previously been used in aqueous- and gas-phase reforming of hydrocarbon and have exhibited improved tolerance toward carbon poisoning [5,8,38–42]. For example, Dumesic and coworkers have shown that the Sn/Ni alloy catalysts are effective in aqueous reforming of oxygenated hydrocarbons [38–40]. In addition, Trimm has reported a number of alloy catalysts, including Sn/Ni, which exhibited enhanced carbon tolerance under steam-reforming conditions [5,8].

Another mechanism by which the growth of carbon networks can be suppressed, explored in detail herein, is to identify those materials that have a low propensity to form carbon nucleation centers. It has been demonstrated previously that carbon nucleation occurs at the undercoordinated Ni sites and that it requires a number of connected Ni sites [37]. By disrupting the connectivity of the undercoordinated Ni sites, the tendency of a material to form carbon nucleation centers can be suppressed. Since the studies presented in Fig. 2 demonstrate that the Sn/Ni

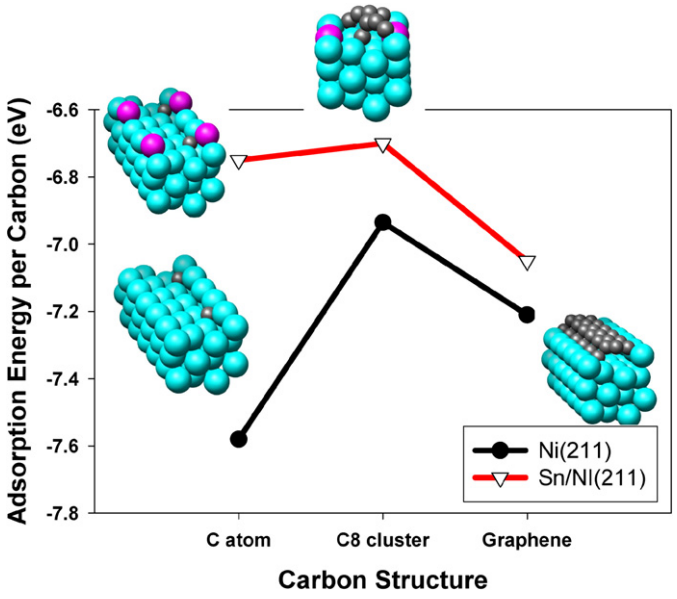

Fig. 3. DFT calculated adsorption energies per carbon atom for a C atom, C_8 cluster, and a graphene chain adsorbed on Ni(211) and Sn/Ni(211), see text. Ni is depicted as a large blue (light), Sn as large magenta and C as small black (dark) atom. The surface alloy is modeled by replacing every third Ni edge atom by Sn.

surface alloy, compared to pure Ni, favors C atom oxidation as opposed to C–C bond formation [34], it is interesting to explore whether the alloying also would have an effect on carbon nucleation. In an attempt to answer this question, we have used DFT calculations to study the adsorption of various carbon structures on undercoordinated Ni and Sn/Ni sites. The carbon nucleation centers were modeled in our DFT calculations as a planar cluster of 8 carbon atoms and as a one-dimensional graphene chain adsorbed on Ni(211) and Sn/Ni(211). We choose the (211) surface termination because it is a good model for the undercoordinated surface sites [43–45]. In the Sn/Ni model system, the Sn atoms displace the Ni edge atoms, as shown in Fig. 3. We comment on the appropriateness of the model system further below.

The DFT-calculated adsorption energies for various carbon structures of Ni and Sn/Ni are shown in Fig. 3. We find that for all carbon examined structures, the undercoordinated sites on Ni(211) bind carbon more strongly than the undercoordinated sites on Sn/Ni(211). For example, the DFT-calculated adsorption energies for the C_8 carbon cluster (8 planar carbon atoms) and a graphene chain on Ni(211) are respectively more exothermic by 0.23 and 0.15 eV per carbon atom than on Sn/Ni(211); see Fig. 3. These results suggest that the undercoordinated sites of Sn/Ni bind the carbon structures less strongly than the identical sites on Ni(211); that is, the thermodynamic driving force to form the carbon nucleation centers is much smaller on Sn/Ni than on Ni. The main reason for this is that Sn breaks the ensembles (ensemble effect) of the low-coordinated Ni atoms, which bind carbon very strongly. It is important to note that whereas the thermodynamic driving force to form carbon nucleation centers is significantly affected with the introduction of Sn the thermodynamic driving force to form CO is changed only slightly. The reason for this is that CO, unlike the extended carbon networks, does not require large ensembles of connected Ni sites.

The DFT studies suggest that a checkerboard Sn/Ni surface alloy, with Sn breaking the connectivity of the Ni surface sites, should concurrently enhance the C atom oxidation and decrease the driving force for the formation of extended carbon networks. Both mechanisms would favorably affect the carbon tolerance of the Ni-based reforming catalysts.

In our DFT calculations we have used the model systems with Sn displacing Ni from the top layer of a Ni slab. It is important to verify whether this model system is thermodynamically feasible.

We have utilized DFT to calculate the formation energies associated with various Sn/Ni alloy structures. The aim of this study was to identify thermodynamically the most stable Sn/Ni configurations for given Sn and Ni concentrations. Since we were interested in perturbing Ni only slightly, we have explored only the structures in the limit of low Sn concentrations. We calculated the formation energy for various Sn/Ni alloy configurations with respect to pure Ni slab using the following expression:

$$E = E(\mathrm{Sn/Ni_{slab}}) - N(\mathrm{Sn})\mu(\mathrm{Sn}) - N(\mathrm{Ni})\mu(\mathrm{Ni}) - E_{\mathrm{formation}}(\mathrm{Ni_{slab}}),$$

$$E_{\mathrm{formation}}(\mathrm{Ni_{slab}}) = E(\mathrm{Ni_{slab}}) - N(\mathrm{Ni_P})\mu(\mathrm{Ni}),$$

where $E(\mathrm{Ni/Sn_{slab}})$ and $E(\mathrm{Ni_{slab}})$ are the DFT calculated energies of an Sn/Ni alloy and a pure Ni slab respectively, $N(\mathrm{Sn})$ and $N(\mathrm{Ni})$ correspond to the number of the Sn and Ni atoms in the alloy slab, $N(\mathrm{Ni_P})$ is the number of Ni atoms in the pure Ni slab, and $\mu(\mathrm{Sn})$ and $\mu(\mathrm{Ni})$ are the respective chemical potentials of Sn and Ni atoms. The chemical potentials of Sn and Ni are functions of the concentration of these atoms in a catalytic particle. In this formulation, a formation energy of zero ($E = 0$) corresponds to the pure Ni slab.

The calculated formation energies (E) for various Sn/Ni structures are plotted in Fig. 4 as a function of Sn surface concentration (the number of Sn atoms in the system divided by the total number of surface atoms in the system). The energies were calculated for (911) fcc surface terminations in a (1×3) unit cell. We utilized this model system since it contains well-coordinated terrace sites and undercoordinated step edge sites. Furthermore, because the unit cell is fairly large, certain terrace and step sites are sufficiently far away from one another so that they are effectively decoupled. This allows us to probe the thermodynamic stability of the structures in which Sn is close to the undercoordinated step edge sites, as well as those structures in which Sn is further away from these sites. The values for $\mu(\mathrm{Sn})$ and $\mu(\mathrm{Ni})$ were obtained in DFT calculations as atomic energies associated with the equilibrium bulk cubic Sn and fcc Ni structures respectively. The identical data are plotted in Fig. 4b; however, instead of the fixed $\mu(\mathrm{Sn})$, the formation energies (E) are calculated for a range of Sn chemical potentials. The structure with the lowest formation energy at a given Sn chemical potential is considered thermodynamically the most stable structure.

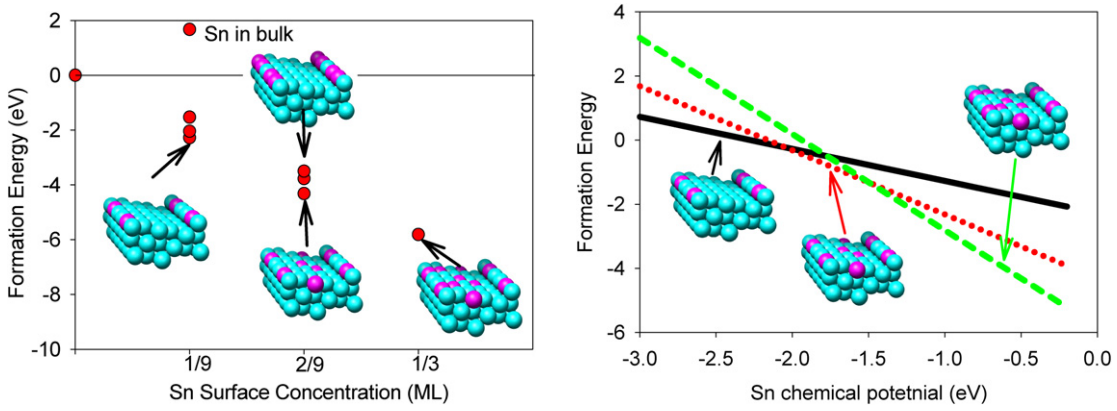

(a) (b)

Fig. 4. (a) DFT-calculated formation energies (see text) for various Sn/Ni configurations are plotted as a function of Sn surface concentration (number of Sn atoms divided by the total number of surface atoms in the unit cell). The structure with the lowest energy is thermodynamically the most stable structure for a given Sn surface concentration. (b) The formation energies of the Sn/Ni configurations are calculated as a function of the Sn chemical potential.

Figs. 4a and 4b show that for very low Sn concentrations (low Sn chemical potential), Sn preferentially displaces the undercoordinated Ni atoms from the Ni edge. Note that not every Ni edge atom is displaced by Sn. For example, in the unit cell that we use in our calculations, the energetically preferred structure has every third Ni edge atom displaced by Sn. The reason for this is that the introduction for a larger number of Sn atoms in the step edge would cause a strain along the step edge, which would increase the energy of the structure. As the concentration of Sn is increased (higher Sn chemical potential), Sn starts to displace the Ni terrace atoms far away from the edge sites. A further increase in the Sn concentration results in further Ni displacement closer to the edge sites. We have also calculated that the formation energy associated with the Sn-induced displacement of the bulk Ni atoms is very high, and that this structure is not stable with respect to the separation of Sn and Ni. In addition, the structures where the Sn atoms are adsorbed on the Ni surface are energetically less favorable than the above-discussed surface alloys. The results shown in Fig. 4 suggest that for low Sn concentrations, the Sn/Ni surface alloy is energetically preferred and that Sn and Ni preferentially assemble in a checkerboard structure, with Sn first displacing the undercoordinated Ni atoms, followed by the displacement of the Ni terrace atoms. This assembly of Sn and Ni is consistent with the model systems used in the DFT studies presented above.

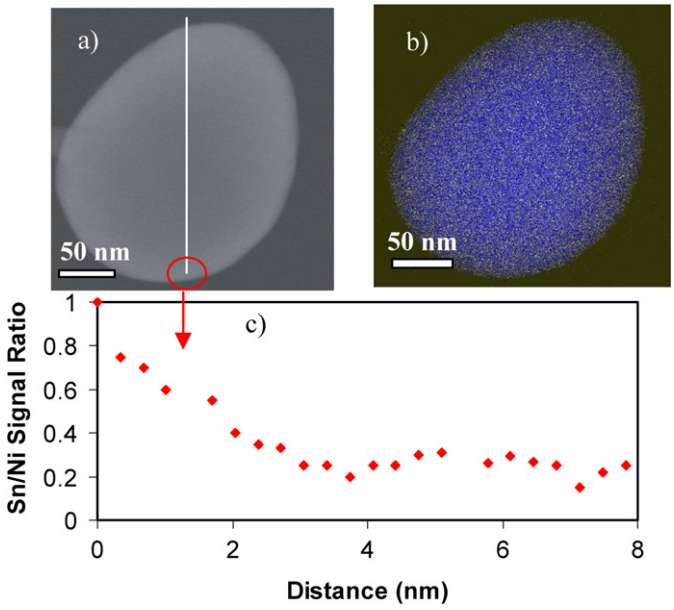

Fig. 5. (a) Scanning transmission electron micrograph of a 1 wt% Sn/Ni/YSZ particle. (b) Energy-dispersive X-ray elemental mapping (EDS) of the Sn/Ni/YSZ particle shows the distribution of Sn and Ni. Ni is depicted by blue (dark) and Sn by yellow (light) pixels. (c) Normalized Sn/Ni ratio (calculated as the ratio divided by the highest measured ratio) measured as a function of the distance from the lowest edge of the particle.

4. Catalyst synthesis and characterization

To test the predictions of the DFT calculations, we have synthesized and characterized Ni/YSZ and Sn/Ni/YSZ catalysts. We tested these catalysts in the steam reforming of methane, propane, and isooctane at different steam-to-carbon ratios. Fig. 5a shows a STEM image of an Sn/Ni particle. Elemental mapping of the Sn/Ni particles supported on YSZ shows that at low Sn loadings [1 wt% with respect to Ni (1 wt% Sn/Ni)], the Sn concentration is highest at the boundaries of the particle. This is most obvious in Fig. 5c, where the ratio of Sn to Ni is measured along a line extending from the edge toward the center of the particle. The EDS line scan shows that the Sn/Ni ratio is highest close to the surface of the particle and that it decreases as the probe moves closer to the center of the particle. This indicates that Sn is located mainly in the surface layers of the particle.

We have also used XPS to characterize the catalysts. The quantified Sn and Ni XP spectra for the 1 wt% Sn/Ni/YSZ catalysts established that the concentration of Sn in the surface layers of the alloy is ∼25%, suggesting that Sn preferentially segregates to the surface of the Sn/Ni alloy. The results of the XPS and EDS studies are consistent with the results of the DFT calculations, which showed that in the limit of low Sn concentrations, the Sn/Ni surface alloy is the thermodynamically preferred structure.

We have also performed TPR experiments. The results of these studies are shown in Fig. 6. TPR was conducted in a stream of 30% H_2/N_2 at a heating rate of 10 K/min. The measured reduction temperature for the 1 wt% Sn/Ni/YSZ catalyst was lower than the reduction temperatures for Ni/YSZ and unsupported Sn. Similar results have been obtained by others [46]. These observations suggest that the alloy binds oxygen with lower adsorption energy than monometallic Sn and Ni. Although it is impossible to determine whether these results are solo due to the surface alloying, our DFT calculations show that the Sn/Ni surface alloy binds oxygen less strongly than pure Ni or Sn. For example, the oxygen atom binding energy for oxygen adsorbed in the fcc threefold hollow sites of Ni(111) is more exothermic (by ∼1.6 eV) than for oxygen adsorbed in the hollow sites on of the Sn/Ni(111) surface alloy. Consequently, the Sn/Ni surface alloy would be expected to undergo the reduction process at a lower temperature than monometallic Ni.

5. Reactor studies

The synthesized catalysts, monometallic Ni supported on YSZ and 1 wt% Sn/Ni alloy supported on YSZ, were tested in the steam reforming of methane, propane, and isooctane. Fig. 7 shows the normalized conversion of methane (measured conversion divided by the highest measured conversion) over the 1 wt% Sn/Ni/YSZ and Ni/YSZ catalysts at a steam-to-carbon ratio of 0.5 and an operating temperature of 1073 K. Fig. 7 shows that the Ni/YSZ catalyst lost ∼45% of its activity after 2 h of operations, whereas the 1 wt% Sn/Ni/YSZ was stable for as long as it was kept on stream (15 h in this case). XRD experiments demonstrated that the Ni/YSZ catalyst deactivated due to the formation of graphitic carbon. The formation of graphitic carbon was not observed for the Sn/Ni alloy catalyst. We have also tested the effect of Sn loading on the catalyst performance and found that as the Sn loading was increased from 1 to 5 wt%, methane conversion was reduced by ∼25%, indicating that an increased Sn concentration has a negative effect on C–H bond activation. Note that the measured steady-state intrinsic rates for 1% Sn/Ni/YSZ were only ∼5% lower than the rates over Ni/YSZ under identical conditions ($T = 1073$ K). This finding is consistent with previous reports [5].

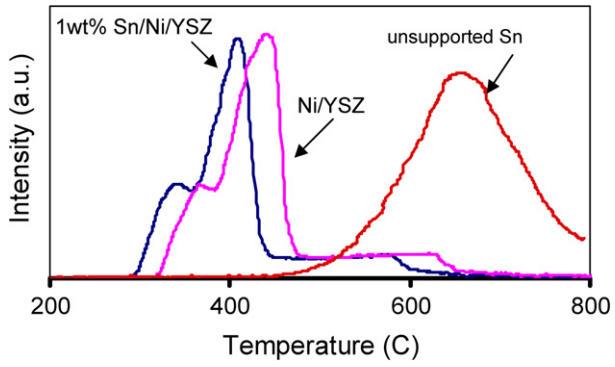

Fig. 6. Temperature-programmed reduction (TPR) spectra for 1 wt% Sn/Ni/YSZ, Ni/YSZ, and an unsupported Sn. Approximately 0.1 g of a catalyst in powder form was used. The catalyst was reduced with a heating rate of 10 K/min and 30% H_2/N_2.

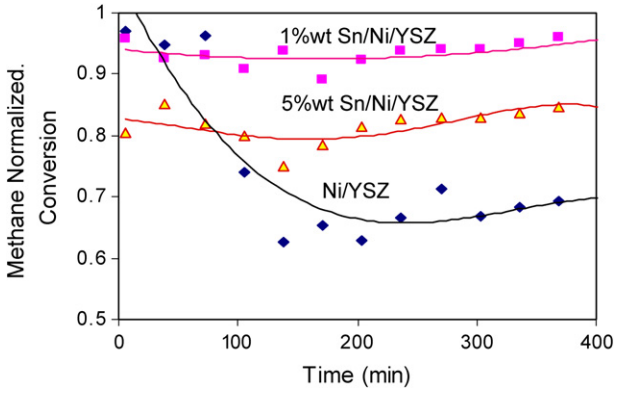

Fig. 7. Normalized methane conversion (methane conversion divided by the highest obtained conversion) as a function of the time on stream for 1 wt% Sn/Ni/YSZ, 5 wt% Sn/Ni/YSZ, and Ni/YSZ catalysts measured at the steam-to-carbon ratio of 0.5 and at 1073 K. The lines are shown only to guide a reader.

We have also tested the catalysts in the steam reforming of propane and isooctane at a steam-to-carbon ratio of 1.5 and an operating temperature of 1073 K. The conversions of propane and isooctane as functions of time on stream are shown in Figs. 8 and 9a, respectively. We observe that for both hydrocarbons, the monometallic Ni catalyst deactivated rapidly under these conditions. The deactivation of Ni was accompanied by a large pressure buildup in the reactor bed, resulting in disintegration of the bed, as corroborated by a visual inspection of the catalyst pellet. We also found that the 1 wt% Sn/Ni alloy catalyst was stable for as long as it was kept on stream (approximately 15 h). The XRD measurements showed that while the graphitic carbon accumulated on the Ni catalyst, no graphitic carbon was detected on the 1 wt% Sn/Ni alloy catalyst; see Fig. 9b. Similar results were obtained for the steam reforming of propane.

We have also analyzed the Ni/YSZ and 1 wt% Sn/Ni/YSZ catalysts used in the steam reforming of isooctane at a steam-to-carbon ratio of 1.5 by XPS. We accounted for any contamination carbon by subtracting the C spectra obtained for a fresh catalyst from the measured spectra associated with the used catalysts. The C 1s XP spectrum for the used Ni/YSZ cata-

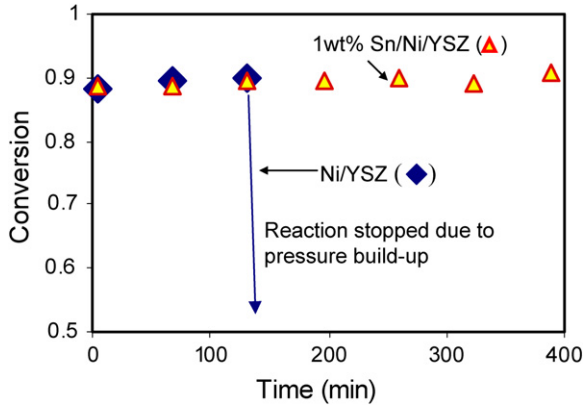

Fig. 8. Propane conversion as a function of the time on stream at a steam-to-carbon ratio of 1.5 and at 1073 K. The arrow indicates the point in time when carbon build-up resulted in the reactor bed disintegration.

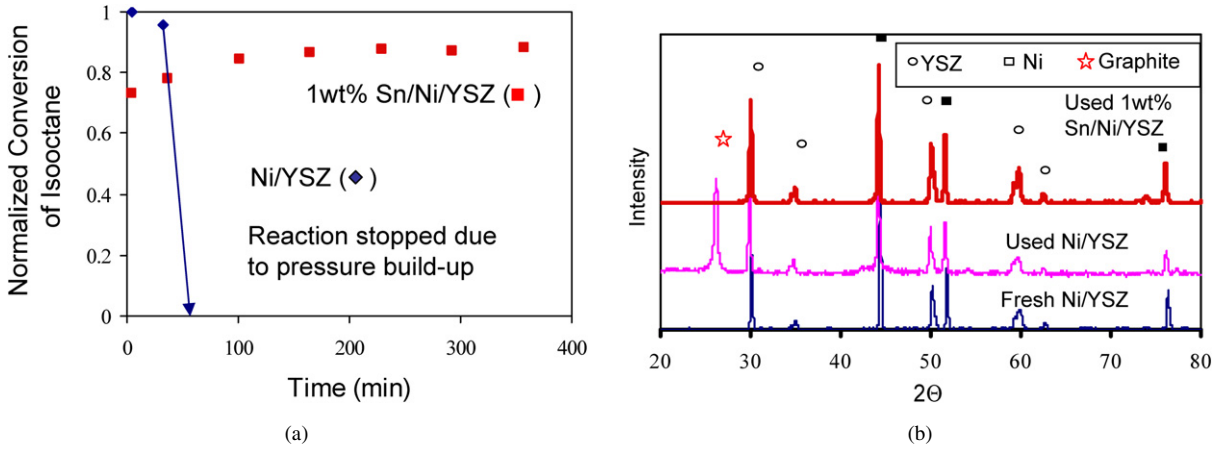

(a) (b)

Fig. 9. (a) Normalized conversion of isooctane (measured isooctane conversion divided by the highest measured conversion) for Ni/YSZ and 1 wt% Sn/Ni/YSZ catalysts at a steam-to-carbon ratio of 1.5 and at 1073 K. (b) XRD spectra for the fresh Ni/YSZ catalyst, used Ni/YSZ, and used 1 wt% Sn/Ni/YSZ.

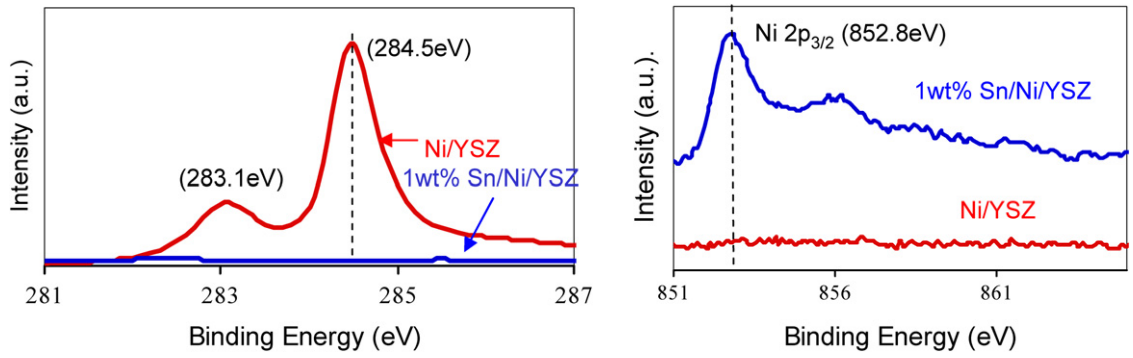

(a) (b)

Fig. 10. The C 1s and Ni $2p_{3/2}$ XP spectra for the Ni/YSZ and 1 wt% Sn/Ni/YSZ catalysts after isooctane steam reforming at a steam-to-carbon ratio of 1.5 and at 1073 K.

lyst revealed two distinguishable carbon peaks, one at 284.5 eV associated with the sp2 carbon and one at 283.1 eV assigned to metal carbide [47,48]. The C 1s XP spectrum for 1 wt% Sn/Ni/YSZ, shown in Fig. 10a, shows no carbon accumulation. It is interesting to note that the amount of carbon deposited on the Ni/YSZ catalyst was so extensive that no Ni signal was detected; that is, Ni was completely covered by the carbon deposits (see Fig. 10b). On the other hand, the Ni XP spectrum associated with the 1 wt% Sn/Ni/YSZ catalyst was identical before and after the reaction.

SEM and TEM characterizations of fresh and used Ni/YSZ and 1 wt% Sn/Ni/YSZ catalysts show that carbon filaments completely covered the used Ni/YSZ catalyst; see Fig. 11a. In contrast, the SEM and TEM images of the used 1 wt% Sn/Ni/YSZ catalysts (Fig. 11b) demonstrate that no carbon structures were formed on Sn/Ni/YSZ.

6. Conclusion

We have used DFT to obtain molecular insights associated with the formation of extended carbon structures on Ni. We have demonstrated that the carbon tolerance of Ni can be improved by formulating Ni-containing surface alloys that, compared with Ni, preferentially oxidize C atoms rather than form C–C bonds and/or have lower a thermodynamic driving force for carbon nucleation on the low-coordinated sites. Using these molecular insights, we have identified Sn/Ni surface alloy as a potential carbon-tolerant reforming catalyst. These predictions are supported by our reactor studies showing that Sn/Ni is much more carbon-tolerant than monometallic Ni in the steam reforming of methane, propane, and isooctane at moderate steam-to-carbon ratios.

Acknowledgments

This work was supported by the DOE-BES, Division of Chemical Sciences (Grant FG-02-05ER15686), the DOE-NETL (Grant FC26-05-NT-42516), and the National Automotive Center. The authors thank SDSC for providing supercomputer time.

References

[1] E. Achenbach, E. Riensche, J. Power Sources 52 (1994) 283.
[2] J.R. Rostrup-Nielsen, J.B. Hansen, S. Helveg, N. Christiansen, A.K. Jannasch, Appl. Phys. A 85 (2006) 427.
[3] J.R. Rostrup-Nielsen, Catalytic Steam Reforming, Catalysis—Science and Technology, Springer-Verlag, Berlin, 1984.
[4] C.M. Finnerty, N.J. Coe, R.H. Cunningham, R.M. Ormerod, Catal. Today 46 (1998) 137.
[5] D.L. Trimm, Catal. Today 49 (1999) 3.
[6] N.C. Triantafyllopoulos, S.G. Neophytides, J. Catal. 217 (2003) 324.

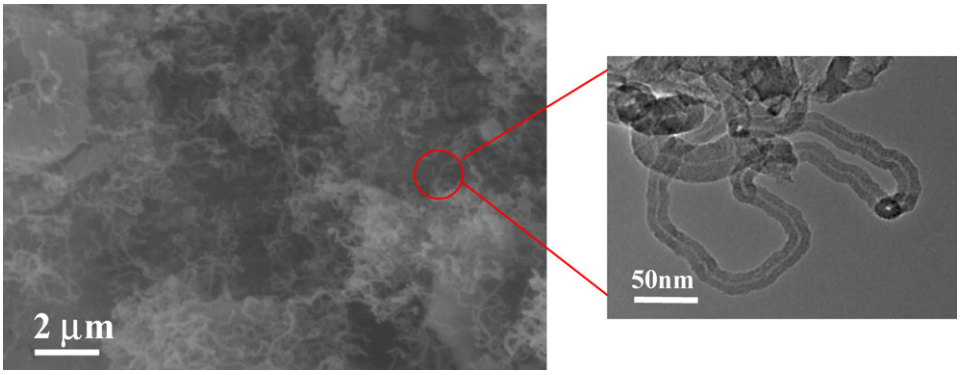

(a)

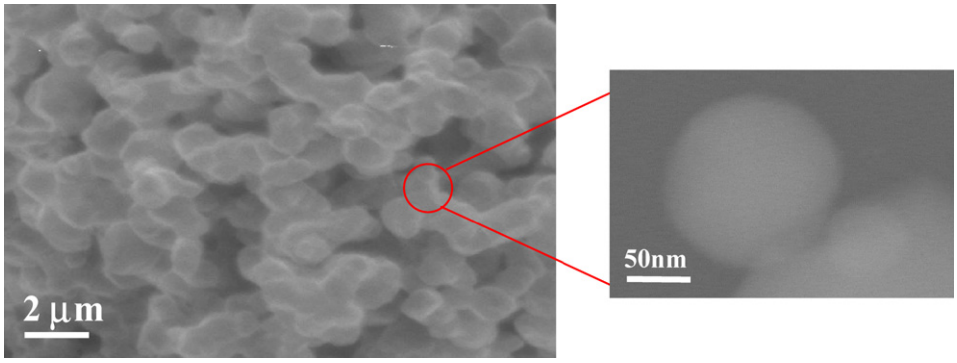

(b)

Fig. 11. (a) SEM and TEM images of Ni/YSZ after isooctane steam reforming at a steam-to-carbon ratio of 1.5 and at 1073 K. The catalyst is completely covered by carbon fibers. (b) SEM and TEM images of 1 wt% Sn/Ni/YSZ after isooctane steam reforming preformed under the identical conditions as in (a). No carbon was detected on the catalyst.

[7] M. Mogensen, K. Kammer, Annu. Rev. Mater. Res. 33 (2003) 321.
[8] D.L. Trimm, Catal. Today 37 (1997) 233.
[9] J. Xu, M. Saeys, J. Catal. 242 (2006) 217.
[10] J.R. Rostrup-Nielsen, L.J. Christiansen, Appl. Catal. A 126 (1995) 381.
[11] T. Takeguchi, Y. Kani, T. Yano, R. Kikuchi, K. Eguchi, K. Tsujimoto, Y. Uchida, A. Ueno, K. Omoshiki, M. Aizawa, J. Power Sources 112 (2002) 588.
[12] J.R. Rostrup-Nielsen, T.S. Christensen, I. Dybkjaer, Recent Adv. Basic Appl. Asp. Ind. Catal. 113 (1998) 81.
[13] J.J. Strohm, J. Zheng, C.S. Song, J. Catal. 238 (2006) 309.
[14] F. Abild-Pedersen, O. Lytken, J. Engbeak, G. Nielsen, I. Chorkendorff, Surf. Sci. 590 (2–3) (2005) 127–137.
[15] J.R. Rostrup-Nielsen, J. Catal. 85 (1) (1984) 31–43.
[16] F. Besenbacher, I. Chorkendorff, B.S. Clausen, A.M. Molenbroek, J.K. Norskov, I. Stensgaard, Science 279 (1998) 1913.
[17] A.M. Molenbroek, J.K. Norskov, B.S. Clausen, J. Phys. Chem. B 105 (2001) 5450.
[18] R.J. Gorte, J.M. Vohs, J. Catal. 216 (2003) 477.
[19] H. Kim, C. Lu, W.L. Worrell, J.M. Vohs, R.J. Gorte, J. Electrochem. Soc. A 149 (2002) 247.
[20] A. Atkinson, S. Barnett, R.J. Gorte, J.T.S. Irvine, A.J. Mcevoy, M. Mogensen, S.C. Singhal, J. Vohs, Nat. Mater. 3 (2004) 17.
[21] M. Mogensen, N.M. Sammes, G.A. Tompsett, Solid State Ionics 129 (2000) 63.
[22] A. Atkinson, Solid State Ionics 95 (1997) 249.
[23] A. Lashtabeg, S.J. Skinner, J. Mater. Chem. 16 (2006) 3161.
[24] V.V. Kharton, F.M. Figueiredo, L. Navarro, E.N. Naumovich, A.V. Kovalevsky, A.A. Yaremchenko, A.P. Viskup, A. Carneiro, F.M.B. Marques, J.R. Frade, J. Mater. Sci. 36 (2001) 1105.
[25] F. Abild-Pedersen, J.K. Norskov, J.R. Rostrup-Nielsen, J. Sehested, S. Helveg, Phys. Rev. B 73 (2006).
[26] R.M. Watwe, H.S. Bengaard, J.R. Rostrup-Nielen, J.A. Dumesic, J.K. Norskov, J. Catal. 189 (2000) 16.
[27] S. Linic, M.A. Barteau, J. Catal. 214 (2003) 200.
[28] S. Linic, J.W. Medlin, M.A. Barteau, Langmuir 18 (2002) 5197.
[29] S. Laursen, S. Linic, Phys. Rev. Lett. 97 (2006).
[30] M. Enever, S. Linic, K. Uffalussy, J.M. Vohs, M.A. Barteau, J. Phys. Chem. B 109 (2005) 2227.
[31] G. Henkelman, B.P. Uberuaga, H. Jonsson, J. Chem. Phys. 113 (2000) 9901.
[32] G. Mills, H. Jonsson, G.K. Schenter, Surf. Sci. 324 (1995) 305.
[33] S. Linic, M.A. Barteau, J. Am. Chem. Soc. 126 (2004) 8086.
[34] E. Nikolla, A. Holewinski, J. Schwank, S. Linic, J. Am. Chem. Soc. 128 (2006) 11354.
[35] H.S. Bengaard, J.K. Norskov, J. Sehested, B.S. Clausen, L.P. Nielsen, A.M. Molenbroek, J.R. Rostrup-Nielsen, J. Catal. 209 (2002) 365.
[36] J.M. Wei, E. Iglesia, J. Catal. 224 (2004) 370.
[37] S. Helveg, C. Lopez-Cartes, J. Sehested, P.L. Hansen, B.S. Clausen, J.R. Rostrup-Nielsen, F. Abild-Pedersen, J.K. Norskov, Nature 427 (2004) 426.
[38] J.W. Shabaker, D.A. Simonetti, R.D. Cortright, J.A. Dumesic, J. Catal. 231 (2005) 67.
[39] J.W. Shabaker, G.W. Huber, J.A. Dumesic, J. Catal. 222 (2004) 180.
[40] G.W. Huber, J.W. Shabaker, J.A. Dumesic, Science 300 (2003) 2075.
[41] C. Padeste, D.L. Trimm, R.N. Lamb, Catal. Lett. 17 (1993) 333.
[42] Z.Y. Hou, O. Yakota, T. Tanaka, T. Yashima, Appl. Surf. Sci. 233 (2004) 58.
[43] B. Hammer, J.K. Norskov, Phys. Rev. Lett. 79 (1997) 4441.
[44] M. Mavrikakis, M. Baumer, H.J. Freund, J.K. Norskov, Catal. Lett. 81 (2002) 153.
[45] V. Pallassana, M. Neurock, L.B. Hansen, J.K. Norskov, J. Chem. Phys. 112 (2000) 5435.
[46] N. Nichio, et al., Catal. Today 62 (2000) 231.
[47] A. Wiltner, C. Linsmeier, Phys. Status Solidi A 201 (2004) 881.
[48] N. Tabet, I. Allam, R.C. Yin, Appl. Surf. Sci. 195 (2002) 166.